Multiphonon Process in Mn-Doped ZnO Nanowires

Jia-Min Lai, Muhammad Umair Farooq, Yu-Jia Sun, Ping-Heng Tan, and Jun Zhang*

Read Online

ACCESS | Metrics & More | Article Recommendations

ABSTRACT: The multiphonon process plays an essential role in understanding electron−phonon coupling, which significantly influences the optical and transport properties of solids. Multiphonon processes have been observed in many materials, but how to distinguish them directly by their spectral characteristics remains controversial. Here, we report high-order Raman scattering up to 10 orders and hot luminescence involving 11 orders of phonons in Mn-doped ZnO nanowires by selecting the excitation energy. Our results show that the intensity distribution of high-order Raman scattering obeys an exponential decrease as the order number increases, while hot luminescence is fitted with a Poisson distribution with a resonance factor. Their linewidth and frequency can be well explained by two different transition models. Our work provides a paradigm for understanding the multiphonon-involved decay process of an excited state and may inspire studies of the statistical characteristics of excited state decay.

KEYWORDS: High-Order Raman Scattering, Hot Luminescence, Electron−Phonon Coupling, ZnO
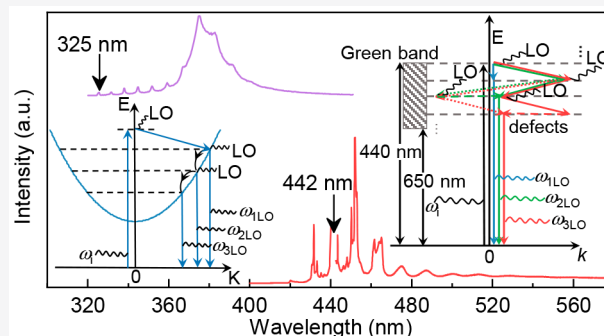
A s scientific interest in many-body interactions in nanomaterials has grown, the electron−phonon interaction has attracted much attention as relates to understanding the decay process of nonequilibrium electrons in matter and developing related optoelectronic and transport devices.[1−7] The multiphonon process as a typical phenomenon induced by strong electron−phonon coupling has been observed in absorption spectra,[8,9] photoluminescence (PL) spectra,[10−12] and scattering spectra.[13−17] For example, the broad-band absorption and emission in the F center are quantitatively explained with the multiphonon transition theory proposed by Huang and Rhys in 1950.[18] They also predicated Poisson-distributed discrete phonon sidebands of the defect center, which was demonstrated in CdS by Hopfield in 1959.[19] In contrast to the usual PL spectrum, radiative recombination of hot electrons in excited states can lead to the hot luminescence process by successively emitting phonons, which reflects the multiphonon transition of electron excited states.[2] Because of the robust Fröhlich interaction[20] between the exciton and the longitudinal optical (LO) phonon, hot luminescence has been widely observed by resonance excitation in group II−VI semiconductors, such as CdS,[11] CdSe,[10] and ZnTe.[12,21] In addition, the multiphonon process can also be dominated by the scattering process, *i.e.* high-order Raman scattering, in which resonance excitation, although not necessary, can significantly enhance the scattering cross section and allow higher-order phonon details to emerge. Both high-order Raman scattering and hot luminescence can even be observed simultaneously,

resulting in misunderstandings in distinguishing them.[22] Menéndez and Cardona stated that in the scattering process the intermediate states are populated during a very short time; thus, the scattering rate is close to the phonon lifetime (~ps), which is far less than the radiation recombination rate.[23] Due to the participation of real electron states in hot luminescence, nonradiative quenching is accessible, while Raman scattering cannot be quenched.[24,25] Martin suggested that the linewidth of the high-order Raman scattering peak is proportional to the order number, which is consistent with the experiments in CsI,[26] while in hot luminescence, the linewidth decreases with increasing order number, which is apparently inconsistent with the previous experiments.[10−12,21] However, there remain rare experiments to distinguish them directly by the spectral characteristics, such as peak frequency and linewidth assessment.

Zinc oxide (ZnO) has served as one of the most promising materials for optoelectronic applications in ultraviolet (UV) regions such as light-emitting diodes, UV lasers, and UV detectors, due to its wide band gap ($E_g \sim 3.37$ eV) and high luminescence efficiency at room temperature.[27−31] Transition-
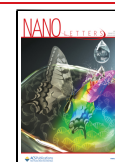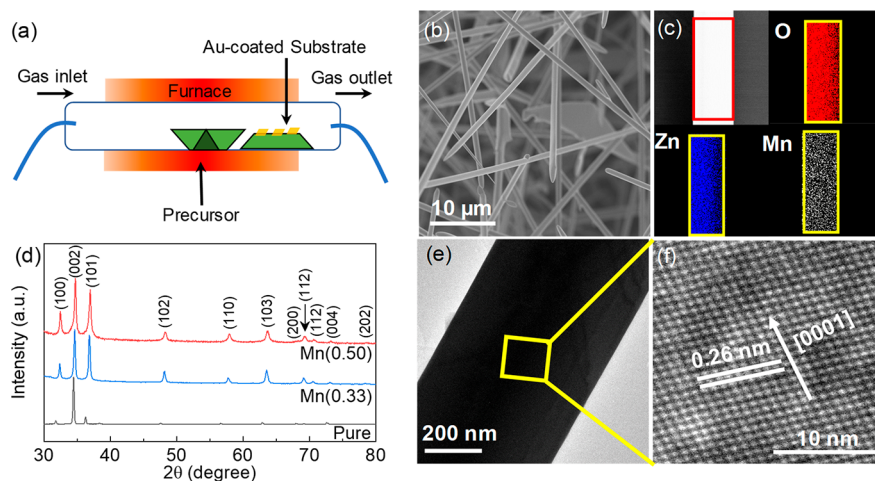
Figure 1. Synthesis and morphology characterization of Mn-doped ZnO. (a) Schematic representation of single-zone CVD. (b) Typical SEM image of Mn-doped ZnO NWs. (c) Mn-doped ZnO NWs and elemental mapping which depicts the distribution of constituents of O, Zn, and Mn. (d) XRD pattern of $Zn_{1-x}Mn_xO$ (x = 0.00, 0.33, and 0.50) NWs. (e) TEM image of an individual NW. The corresponding HRTEM in the yellow region is shown in part f.

metal-doped (*e.g.* Co, Mn, etc.) ZnO shows high-temperature ferromagnetism for the potential applications of spintronic devices.[32,33] The large exciton binding energy (~60 meV) at room temperature[34] makes ZnO an ideal platform to explore the exciton−phonon interaction. The strong exciton−phonon interaction is sometimes depicted by a quasi-particle model, namely a polaron.[35,36] It has been predicted that the number of multi-LO-phonon lines in ZnO would be higher than that of CdS with 9LO phonon peaks,[11] since ZnO has a larger exciton−phonon coupling strength.[37] In previous experiments, 11LO phonon peaks have been observed with excitation energy larger than the band gap in Cu, Ni-doped ZnO,[38,39] while in Mn-doped ZnO, only 5LO phonon peaks were measured.[40,41] In a ZnO nanostructure with minor Mn doping, Liu et al. observed phonon-assisted stimulated emission indicating the strong electron−phonon coupling in Mn-doped ZnO and the potential applications for UV lasers.[31] Besides, high-order Raman scattering remains rarely reported in ZnO. Here, we observed both high-order Raman scattering and hot luminescence in Mn-doped ZnO by selecting the excitation energy. We clarify the spectral characteristics in these processes and explain them by specific transition models, which are also applicable to multiphonon processes in other materials.

Mn-doped ZnO nanowires (NWs) were grown by a typical chemical vapor deposition (CVD) method, as shown in Figure 1a. Well-mixed ZnO (99.99%, Aladdin) and Mn(II) (99.9%, Alfa Aesar) powders with the molar ratio of $Zn_{1-x}Mn_xO$ (x = 0.00, 0.33, and 0.50) were taken into a ceramic boat and then placed into a quartz tube mounted on a horizontal tube furnace. Several pieces of Si(100) substrates were ultrasonically cleaned by acetone, ethanol, and deionized water for 15 min each. The ultrasonically clean substrates were coated with a Au film of 10 nm thickness by a thermal beam evaporation system. To get highly smooth and homogeneous nanowires, the substrates were placed into the quartz tube 10 cm away from the heating zone center. First, a 100 sccm flow of Ar gas was introduced into the tube furnace for 30 min to eject out the air and other contaminants. Then, the temperature of the CVD was adjusted from room temperature to 1050 °C for 90 min. When the temperature of the CVD rose to 720 °C, O_2 and H_2

gases were introduced at flow rates of 10 and 10 sccm, respectively. Simultaneously, the flow rate of Ar was increased to 300 sccm. After that, the CVD instrument was naturally cooled down to room temperature with an Ar gas flow. A yellow nanowire can be obtained on the Si substrate with high density.

The crystal structures of as-synthesized Mn-doped nanowires were investigated by X-ray powder diffraction (XRD, Philips X'Pert Pro MPD with a Cu Kα radiation source (λ = 0.15418 nm). The surface morphology of the nanowires was examined by scanning electron microscopy (SEM, Zeiss Supra 55) and transmission electron microscopy (TEM, FEI Tecnai T20, and F30). The elemental composition of the nanowires was analyzed by energy-dispersive X-ray spectroscopy (EDS) equipped with SEM. For Raman and photoluminescence (PL) experiments, the as-grown sample was ultrasonicated to remove the NWs from the Si(100) substrates to an ethanol solvent and dropped-cast onto another Si substrate. Raman and PL spectra were conducted at room temperature using a Jobin-Yvon HR800 system equipped with a liquid-nitrogen-cooled charge-coupled detector (CCD). The PL and Raman spectra were collected with a 100× objective lens (NA = 0.9) and 600 lines/mm and 100 lines/mm gratings. A series of laser lines 325 nm (He-Cd laser), 355 nm (DPSS laser), 405 nm (semiconductor laser), and 442 nm (He-Cd laser) were used as the excitation sources.

The representative SEM image (Figure 1b) result shows that the well-grown ZnO NWs have a uniform diameter along their entire length and the diameters are about 1 μm. The EDS result of Mn-doped NWs as shown in Figure 1c indicates that Mn^{2+} ions have been successfully incorporated into the ZnO lattice without forming any clusters or defect centers. Mn^{2+} is detected in each sample with a small concentration (0.5%, wt %); hence, we cannot determine the Mn^{2+} concentration in ZnO when the amount of Mn was changed during synthesis. All the diffraction peaks (Figure 1d) in the XRD patterns are well-matched with the wurtzite hexagonal structure of ZnO (JCPDS Card No. 076-0703). Compared with the pure ZnO, the variation of the relative intensities and the broad linewidths of the diffraction peaks of Mn-doped ZnO indicate that the addition of Mn dopants will affect the crystal orientation and
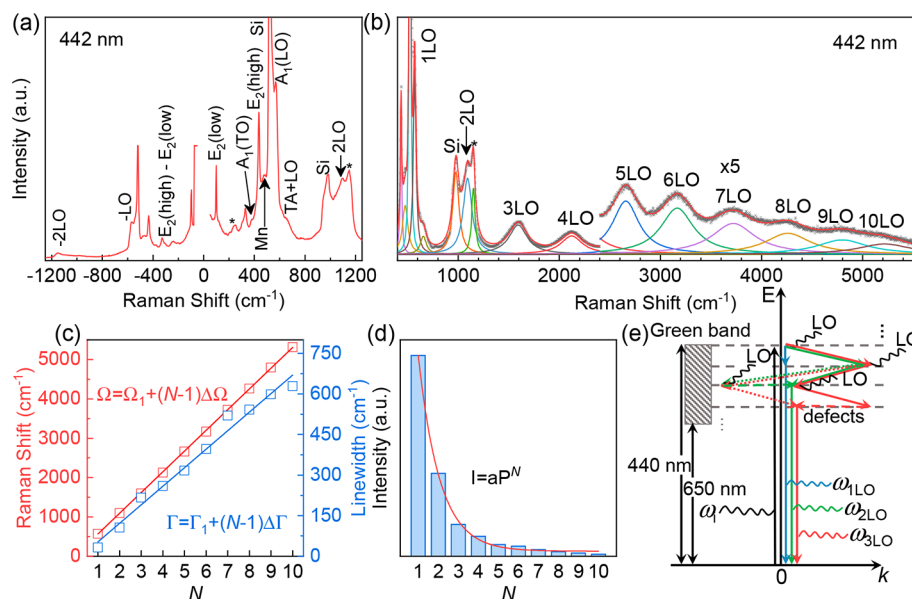
Figure 2. High-order phonon Raman scattering of Mn-doped ZnO NWs. (a) Raman spectrum of Mn-doped ZnO excited by a 442 nm laser. The stars mark unknown phonon modes. The corresponding higher wavenumber Raman spectrum with subtraction of the green band PL background is shown in part b. Lorentzian profiles are fitted to the LO phonon from N = 1 to 10 order. (c) Order number N dependence of the Raman shift Ω and the linewidth Γ of the LO phonons. The solid lines denote linear fitting results. (d) Intensities of the NLO Raman modes as a function of N. The red line is the exponential fitting result. (e) Schematic diagram of the high-order Raman scattering. The black, blue, green, and red arrows represent the incident laser (ω_i), 1LO, 2LO, and 3LO scattering processes, respectively. The dashed arrows denote the elastic scattering by the defects. The dotted arrows denote other possible scattering paths.

crystallization degree of ZnO. The TEM result (Figure 1e) of the Mn-doped ZnO sample reveals smooth and uniform NWs, which is consistent with the SEM patterns. Furthermore, the high-resolution TEM (HRTEM) lattice image (Figure 1f) confirms that the highly crystalline planes of NWs are well separated by a spacing of d = 0.26 nm with the [0001] direction.

Wurtzite ZnO belongs to the C_{6v}^4 point group with six irreducible zone-center optical phonon modes denoted by[42] $\Gamma_{opt} = A_1 + 2B_1 + E_1 + 2E_2$. Among them, the A_1 and E_1 modes are from an anisotropy-induced splitting of the F mode from the zinc-blende Γ-point, while $2B_1$ and $2E_2$ are from the backfolding of the zinc-blende zone-edge modes. The B_1 modes are silent modes, and the A_1 and E_1 modes are polar modes, which are both Raman and infrared active, whereas the E_2 modes are nonpolar Raman active only. Figure 2a shows a typical Raman spectrum of an individual Mn-doped ZnO NW. The peaks centered at 99, 330, 377, 435, 570, 655, and 1094 cm^{-1} are attributed to the E_2(low), E_2(high) − E_2(low), A_1(TO), E_2(high), A_1(LO), TA + LO, and $2A_1$(LO) modes, respectively.[43] The phonon mode centered at 477 cm^{-1} may be attributed to the surface/interface phonon mode[40] or to two-phonon processes in the disordered lattice due to the incorporation of Mn^{2+}.[39,44,45]

We observed high-order Raman scattering up to the 10LO phonon with 442 nm excitation below the Mn-doped ZnO band gap ($\sim$3.26 eV, 380 nm), as shown in Figure 2b. By fitting the spectrum, we found that both the Raman shift and the linewidth show a linear dependence on the order number N with a nonzero intercept (Figure 2c). Considering momentum conservation, this high-order Raman scattering can be well explained by the model in Figure 2e: In the first order scattering, the excited electron is scattered by one phonon at the center of the Brillouin zone ($q_1 \sim 0$) to a virtual

state followed by photon emitting, while, for the second order scattering, the excited electron is scattered with release of a phonon with a wave vector of $q_1 = q \neq 0$, and then the other phonon ($q_2 = -q$) scatters the electron back followed by photon emitting. During the third order scattering, the participating phonons own wave vectors of $q_1 = q$, $q_2 = -q$, and $q_3 = q$, and the electron is inelastically scattered back by the defects, where the electron momentum changes by $-q$, and so on, in the Nth order Raman scattering, ($N - 1$) phonons with a nonzero wave vector are involved in the scattering process. Here, the electron state probably originates from the well-known green band induced by the defects related to oxygen atoms.[29] Note that other paths also may involve the scattering process. For example, in the second order scattering, the excited electron was scattered by the phonons with $q_1 = q$ and $q_2 = -2q$ (as shown by the green dotted arrows in Figure 2e) and then elastically scattered back by the defects. The third order scattering process shown by the red dotted arrows may also occur. These processes will increase the frequency uncertainty of the scattering peak, leading to linewidth broadening. Considering that each phonon with a nonzero wave vector increases the linewidth by $\Delta\Gamma$, the order number dependence of the Raman linewidth can be fitted by $\Gamma = \Gamma_1 + (N - 1)\Delta\Gamma$, where $\Delta\Gamma = 68 \pm 3$ cm^{-1} and $\Gamma_1 = 53 \pm 8$ cm^{-1} is the linewidth of the 1LO phonon peak (Figure 2c). A similar result also was observed in CsI.[26] Besides, except for the first phonon, all the phonons come from the noncenter of the Brillouin zone. Considering the LO phonon dispersion which is near-flat at the center of the Brillouin zone but slightly decreased as the wave vector increases, we deduce that the frequency of the first phonon (Ω_1) is slightly higher than those of the others ($\Delta\Omega$). Consequently, the Raman shift can be fitted with $\Omega = \Omega_1 + (N - 1)\Delta\Omega$, where $\Omega_1 = 568 \pm 6$ cm^{-1} is larger than $\Delta\Omega = 526 \pm 2$ cm^{-1}. The scattering probability P
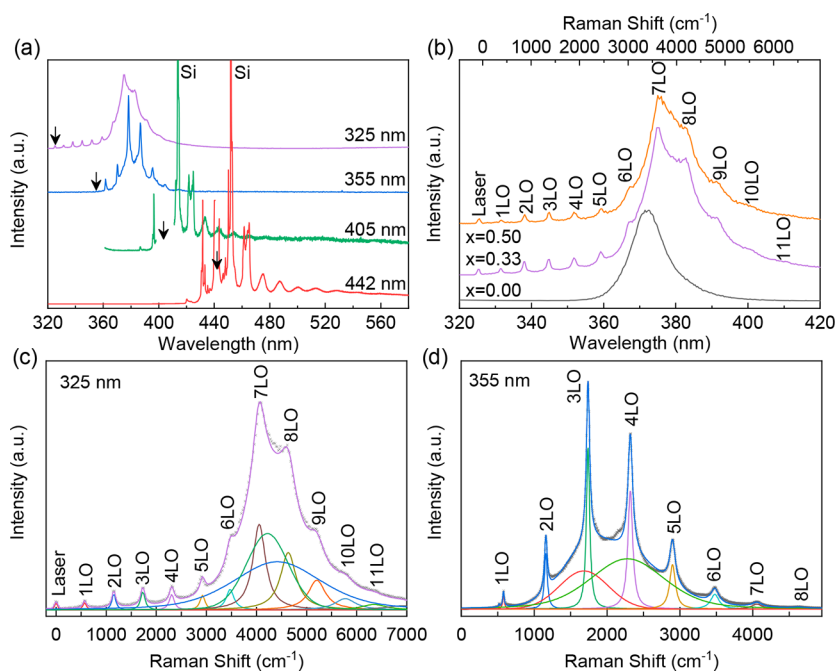
Figure 3. Hot luminescence spectra of Mn-doped ZnO NWs. (a) Spectra excited by different wavelength lasers. (b) Hot luminescence spectra of $Zn_{1-x}Mn_xO$ (x = 0.00, 0.33, and 0.50) excited by a 325 nm laser. (c) 325 nm and (d) 355 nm excitation and the corresponding fitting results. The x-axis shows the relative frequency shift by offsetting the laser frequency to zero.
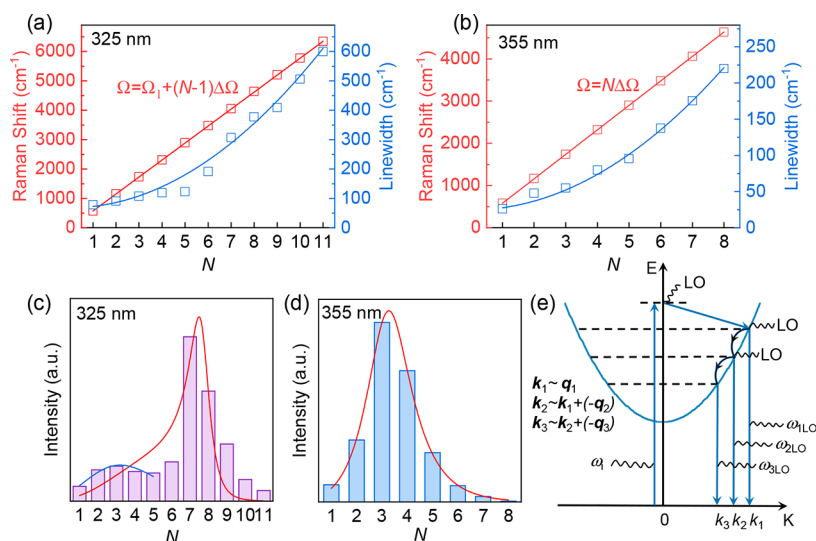

Figure 4. Cascade model of hot luminescence in Mn-doped ZnO NWs. Phonon peak frequency Ω and the line width Γ extracted from spectra excited by (a) 325 nm and (b) 355 nm. The red and blue lines denote the linear fitting of the frequency and the parabolic fitting of the line width, respectively. Parts c and d are the fitted intensities from spectra excited by 325 and 355 nm, respectively. (e) Schematic diagram of the cascade model. Notice that k_1, k_2, and k_3 are the wave vectors of the photons with NLO phonon emissions and q_1, q_2, and q_3 are the phonon wave vectors.

determines the intensities of the phonon peaks, which can be fitted by $I = aP^N$ as shown in Figure 2d, where $P = 0.34 \pm 0.01$ means the probability of scattering one phonon and a is a coefficient of intensity. This exponential decay reflects the scattering probability dependence between $(N + 1)^{th}$ and N^{th} order, indicating that the phonon scattering channels are sequential and correlated.

To further investigate the electron−phonon interaction in Mn-doped ZnO, we measured the spectra with different excitation energies. As shown in Figure 3a, when excited below the ZnO band gap, high-order Raman scattering as discussed above is observed without an apparent PL background.

However, when the excitation (355 and 325 nm) is larger than the band gap, the multiphonon featured PL spectra can be measured. In the Raman spectrum (Figure 2a), both Stokes and anti-Stokes signals can be measured, while in Figure 3b, only the Stokes signal of the LO phonon mode can be observed because the electrons interact more strongly with LO phonons than with other phonon modes. In polar crystals, the LO phonons involve relative displacement of oppositely charged atoms and induce an oscillating macroscopic polarization which strongly interacts with the electrons via the Fröhlich interaction.[20] Eleven orders of LO phonon modes are observed in Mn-doped samples (Figure 3b), which is much

higher than the five orders in previous reports.[38−41] The deformation potential of ion doping influences the atom displacement from the equilibrium position,[31,46] which enhances the lattice polarity and the electron−phonon interaction. The low doping concentration of Mn^{2+} induces the red shift of the band edge caused by the *sp-d* exchange interaction between the localized *d* electron of Mn^{2+} and group VI anions,[45,47,48] which increases the energy difference between the excitation laser and the band edge and leads to higher-order phonons involved in the resonance. Besides, Mn^{2+} can strongly quench the band gap emission due to the radiative absorption by color centers and trapping of electrons by defects centers;[38] thus, such high-order phonon peaks can be observed. The multiphonon peaks under 325 and 355 nm excitation can be well fitted by Lorentzian profiles as shown in Figure 3c and d. The PL background is fitted by two PsdVoigt profiles (linear combination of Gaussian and Lorentzian line shapes), which are from the band edge emission and the free exciton near the band edge.

Then we discuss the fundamental difference between this multiphonon featured PL and the high-order Raman scattering. The frequency, linewidth, and intensity distribution of the multiphonon peaks are shown in Figure 4a−d. It is noted that the intensity distributions in these two spectra show an obvious enhancement at the exciton resonant energy rather than the exponential decay observed in high-order Raman scattering (Figure 2d). This multiphonon PL process is attributed to the hot luminescence process depicted by the cascade model[49] in Figure 4e: First, the incident laser excites a virtual state. Then, the electron is scattered to the real exciton state with an LO phonon emission. Next, the real exciton relaxes in the excited state with an emission LO phonon in succession. After each phonon emission, the excited electron has a probability of radiating back to the ground state. Therefore, the wave vector of the first LO phonon is larger than those of the other phonons. Considering the LO phonon dispersion which is normally near-flat at the center of the Brillouin zone but slightly decreased as the wave vector increases, the frequency of the first LO phonon (Ω_1) is slightly smaller than those of the higher-order phonons ($\Delta\Omega$). Figure 4a shows the linear fitting ($\Omega = \Omega_1 + (N-1)\Delta\Omega$) of frequency at 325 nm excitation that yields a slope of 578.0 ± 0.7 cm^{-1} and Ω_1 of 571 ± 3 cm^{-1}, which supports the above hot luminescence process. Unlike high-order Raman scattering, here the order number dependence of the phonon linewidth is parabolic, which is related to the parabolic dependence of the exciton energy on the wave vector. With the order number increasing, for the same energy change, the wave vector of the phonon increases, resulting in a larger uncertainty of the frequency. Compared with the scattering process, in the luminescence process, the intermediate state is populated for a longer time;[1] thus, the interaction of the surroundings may destroy the coherence of the phonons. As the order number increases, more phonons in different directions participate, and the uncertainty of the frequency increases, which also leads to linewidth broadened. We note that the frequency at the 355 nm excitation can be fitted well by $\Omega = N\Delta\Omega$ (where $\Delta\Omega = 579.7 \pm 0.3$ cm^{-1}), suggesting that the incident laser also can vertically excite the exciton state with $k \neq 0$, where momentum conservation is achieved by electron−hole recombination.

The emission intensity distribution of multiphonon peaks is determined by the density of the excited states and the electron−phonon coupling strength. In general, the electron−

phonon coupling strength can be evaluated by the Huang−Rhys factor S which was first proposed in defect centers, where the lattice relaxation causes the equilibrium atom position of the final state to shift from the initial state, leading to the multiphonon side band emission.[18] In defect centers, the phonon side band emission channels are independent of each other; thus, the intensity distribution obeys the Poisson distribution[18] $I_N = I_0 \frac{e^{-S}S^N}{N!}$, where I_0 is the intensity of the original electronic band. Analogously, considering the outgoing resonance with the exciton, we modify the intensity distribution in hot luminescence with a resonance factor: $I_N = I_0 e^{-S}\frac{S^N}{N!}\frac{1}{(E_i - E_{ex} - NE_{LO})^2 + \kappa^2}$, where E_i, E_{ex}, and E_{LO} are the energies of the incident laser, exciton, and LO phonon, respectively, and κ is the damping factor of the exciton. We note that in the spectrum with 325 nm excitation, when the phonon order N is <6 where the PL background is weak enough to ignore, the intensity of the phonon peaks satisfies the Poisson distribution (blue curve in Figure 4c) well and the S factor is 3.7 ± 0.2, while when $N \geq 6$, the exciton resonance must be taken into consideration (red curve in Figure 4c). Similarly, in the spectrum with the 355 nm excitation, the whole of the phonon peaks can be well fitted considering the resonance factor and the S factor is 4.2 ± 0.1 as shown in Figure 4d. It should be noted that the S factor is largely influenced by the sample structure, excitation energy, excitation power, measurement temperature, and even different calculated methods; hence, the investigation of the electron−phonon coupling strength is required to be carried out under the same conditions.[50]

In conclusion, we investigate the multiphonon process in Mn-doped ZnO NWs with different excitation energies. When they are excited below the band gap, high-order Raman scattering can be observed, while when they are excited above the band gap, hot luminescence is dominant. Both processes depend on the strong electron−phonon interaction, but the essential difference between them is that the high-order Raman scattering reflects the properties of the vibration state scattered by the exciton while the hot luminescence directly reveals the radiative recombination of the exciton excited state by releasing phonons. The different spectral characteristics can be explained by two different transition models, which also can be extended to other materials with strong electron−phonon interactions. The different intensity distributions reveal the dependence among the phonon scattering channels or the independence among the phonon emission channels of excited state decay and reflect profound macroscopic statistical characteristics in quantum many-body systems involved with phonons, excitons, and photons.

■ AUTHOR INFORMATION

Corresponding Author

Jun Zhang − *State Key Laboratory of Superlattices and Microstructures, Institute of Semiconductors, Chinese Academy of Sciences, Beijing 100083, China; Center of Materials Science and Optoelectronics Engineering and CAS Center of Excellence in Topological Quantum Computation, University of Chinese Academy of Sciences, Beijing 100049, China;* ⓞ orcid.org/0000-0002-9831-6796;
Email: zhangjwill@semi.ac.cn

Authors

Jia-Min Lai − *State Key Laboratory of Superlattices and Microstructures, Institute of Semiconductors, Chinese Academy of Sciences, Beijing 100083, China; Center of Materials Science and Optoelectronics Engineering, University of Chinese Academy of Sciences, Beijing 100049, China*

Muhammad Umair Farooq − *State Key Laboratory of Superlattices and Microstructures, Institute of Semiconductors, Chinese Academy of Sciences, Beijing 100083, China; Institute of Physics, The Islamia University of Bahawalpur, Bahawalpur 63100, Pakistan*

Yu-Jia Sun − *State Key Laboratory of Superlattices and Microstructures, Institute of Semiconductors, Chinese Academy of Sciences, Beijing 100083, China; Center of Materials Science and Optoelectronics Engineering, University of Chinese Academy of Sciences, Beijing 100049, China*

Ping-Heng Tan − *State Key Laboratory of Superlattices and Microstructures, Institute of Semiconductors, Chinese Academy of Sciences, Beijing 100083, China; Center of Materials Science and Optoelectronics Engineering, University of Chinese Academy of Sciences, Beijing 100049, China;* orcid.org/0000-0001-6575-1516

Complete contact information is available at:
https://pubs.acs.org/10.1021/acs.nanolett.2c01428

Author Contributions

J.Z. conceived the project. J.L., M.U.F., and Y.S. performed experiments. J.L. and J.Z. analyzed the data and wrote the paper. All of the authors discussed the results and revised the paper.

Funding

Notes

The authors declare no competing financial interest.

■ REFERENCES

(1) Weisbuch, C.; Ulbrich, R. G. Resonant light scattering mediated by excitonic polaritons in semiconductors. In *Light Scattering in Solids III: Recent Results*; Cardona, M., Güntherodt, G., Eds.; Springer Berlin Heidelberg: Berlin, Heidelberg, 1982; pp 207−263.

(2) Yu, P. Y.; Cardona, M. Optical Properties II. In *Fundamentals of Semiconductors*; Yu, P. Y., Cardona, M., Eds.; Springer Berlin Heidelberg: Berlin, Heidelberg, 2010; pp 345−426.

(3) Lai, J.-M.; Xie, Y.-R.; Zhang, J. Detection of electron-phonon coupling in two-dimensional materials by light scattering. *Nano Res.* **2021**, *14* (6), 1711−1733.

(4) Schlipf, M.; Ponce, S.; Giustino, F. Carrier Lifetimes and Polaronic Mass Enhancement in the Hybrid Halide Perovskite $CH_3NH_3PbI_3$ from Multiphonon Frohlich Coupling. *Phys. Rev. Lett.* **2018**, *121* (8), No. 086402.

(5) Kilina, S. V.; Neukirch, A. J.; Habenicht, B. F.; Kilin, D. S.; Prezhdo, O. V. Quantum Zeno effect rationalizes the phonon bottleneck in semiconductor quantum dots. *Phys. Rev. Lett.* **2013**, *110* (18), 180404.

(6) Pandey, J.; Soni, A. Unraveling biexciton and excitonic excited states from defect bound states in monolayer MoS2. *Appl. Surf. Sci.* **2019**, *463*, 52−57.

(7) Pandey, J.; Soni, A. Electron-phonon interactions and two-phonon modes associated with charge density wave in single crystalline 1T−VSe₂. *Phys. Rev. Res.* **2020**, *2* (3), No. 033118.

(8) Seong, M. J.; Miotkowski, I.; Ramdas, A. K. Oxygen isoelectronic impurities in ZnTe: Photoluminescence and absorption spectroscopy. *Phys. Rev. B* **1998**, *58* (12), 7734−7739.

(9) Gourley, J. T.; Runciman, W. A. Multiphonon Infrared-Absorption Spectra of MgO and CaO. *J. Phys. C: Solid State Phys.* **1973**, *6* (3), 583−592.

(10) Galak, M.; Dmitruk, I. Hot luminescence of CdSe nanoparticles at low temperature. *J. Lumin.* **2005**, *112* (1−4), 166−168.

(11) Leite, R. C. C.; Scott, J. F.; Damen, T. C. Multiple-Phonon Resonant Raman Scattering in CdS. *Phys. Rev. Lett.* **1969**, *22* (15), 780−782.

(12) Zhang, Q.; Liu, X.; Utama, M. I.; Zhang, J.; de la Mata, M.; Arbiol, J.; Lu, Y.; Sum, T. C.; Xiong, Q. Highly enhanced exciton recombination rate by strong electron-phonon coupling in single ZnTe nanobelt. *Nano Lett.* **2012**, *12* (12), 6420−6427.

(13) Wang, R. P.; Zhou, G. W.; Liu, Y. L.; Pan, S. H.; Zhang, H. Z.; Yu, D. P.; Zhang, Z. Raman spectral study of silicon nanowires: High-order scattering and phonon confinement effects. *Phys. Rev. B* **2000**, *61* (24), 16827−16832.

(14) Tan, P. H.; Hu, C. Y.; Dong, J.; Shen, W. C.; Zhang, B. F. Polarization properties, high-order Raman spectra, and frequency asymmetry between Stokes and anti-Stokes scattering of Raman modes in a graphite whisker. *Phys. Rev. B* **2001**, *64* (21), 214301.

(15) Wang, F.; Liu, W.; Wu, Y.; Sfeir, M. Y.; Huang, L.; Hone, J.; O'Brien, S.; Brus, L. E.; Heinz, T. F.; Shen, Y. R. Multiphonon Raman scattering from individual single-walled carbon nanotubes. *Phys. Rev. Lett.* **2007**, *98* (4), No. 047402.

(16) Dashwood, C. D.; Geondzhian, A.; Vale, J. G.; Pakpour-Tabrizi, A. C.; Howard, C. A.; Faure, Q.; Veiga, L. S. I.; Meyers, D.; Chiuzbăian, S. G.; Nicolaou, A.; Jaouen, N.; Jackman, R. B.; Nag, A.; García-Fernández, M.; Zhou, K.-J.; Walters, A. C.; Gilmore, K.; McMorrow, D. F.; Dean, M. P. M. Probing Electron-Phonon Interactions Away from the Fermi Level with Resonant Inelastic X-Ray Scattering. *Phys. Rev. X* **2021**, *11* (4), No. 041052.

(17) Zacharias, M.; Seiler, H.; Caruso, F.; Zahn, D.; Giustino, F.; Kelires, P. C.; Ernstorfer, R. Efficient First-Principles Methodology for the Calculation of the All-Phonon Inelastic Scattering in Solids. *Phys. Rev. Lett.* **2021**, *127* (20), 207401.

(18) Huang, K.; Rhys, A. Theory of Light Absorption and Non-Radiative Transitions in F-Centres. *Proceedings of the Royal Society of London Series A-Mathematical and Physical Sciences* **1950**, *204* (1078), 406−423.

(19) Hopfield, J. J. A Theory of Edge-Emission Phenomena in Cds, ZnS and ZnO. *J. Phys. Chem. Solids* **1959**, *10* (2−3), 110−119.

(20) Yu, P. Y.; Cardona, M. Vibrational Properties of Semiconductors, and Electron-Phonon Interactions. In *Fundamentals of Semiconductors*; Yu, P. Y., Cardona, M., Eds.; Springer Berlin Heidelberg: Berlin, Heidelberg, 2010; pp 107−158.

(21) Zhang, Q.; Zhang, J.; Utama, M. I. B.; Peng, B.; de la Mata, M.; Arbiol, J.; Xiong, Q. H. Exciton-phonon coupling in individual ZnTe nanorods studied by resonant Raman spectroscopy. *Phys. Rev. B* **2012**, *85* (8), No. 085418.

(22) Tanino, H.; Kobayashi, K. Relaxation of Electron-Phonon System in Optically Excited Quasi-1-D Mixed Valence Crystal Wolffram's Red Salt. *J. Phys. Soc. Jpn.* **1983**, *52* (4), 1446−1456.

(23) Menéndez, J.; Cardona, M. Interference effects: A key to understanding forbidden Raman scattering by LO phonons in GaAs. *Phys. Rev. B Condens Matter* **1985**, *31* (6), 3696−3704.

(24) Fouche, D. G.; Chang, R. K. Observation of Resonance Raman Scattering below the Dissociation Limit in I₂ Vapor. *Phys. Rev. Lett.* **1972**, *29* (9), 536−539.

(25) Permogorov, S. Hot Excitons in Semiconductors. *Phys. Status Solidi B* **1975**, *68* (1), 9−42.

(26) Martin, T. P. Multiple-Order Raman-Scattering by a Localized Mode. *Phys. Rev. B* **1976**, *13* (8), 3617−3622.

(27) Wang, X.; Ye, H.; Su, Z.; Yu, D.; Xu, S. Observation of two-times self-focusing of femtosecond laser beam in ZnO crystal by two-photon luminescence. *Sci. Bull.* **2018**, *63* (21), 1392−1396.

(28) Galdamez-Martinez, A.; Santana, G.; Guell, F.; Martinez-Alanis, P. R.; Dutt, A. Photoluminescence of ZnO Nanowires: A Review. *Nanomaterials* **2020**, *10* (5), 857.

(29) Özgür, Ü.; Alivov, Y. I.; Liu, C.; Teke, A.; Reshchikov, M. A.; Dogan, S.; Avrutin, V.; Cho, S. J.; Morkoc, H. A comprehensive review of ZnO materials and devices. *J. Appl. Phys.* **2005**, *98* (4), No. 041301.

(30) Borysiewicz, M. A. ZnO as a Functional Material, a Review. *Crystals* **2019**, *9* (10), 505.

(31) Liu, R. B.; Pan, A. L.; Fan, H. M.; Wang, F. F.; Shen, Z. X.; Yang, G. Z.; Xie, S. S.; Zou, B. S. Phonon-assisted stimulated emission in Mn-doped ZnO nanowires. *J. Phys.: Condens. Matter* **2007**, *19* (13), 136206.

(32) Sharma, P.; Gupta, A.; Rao, K. V.; Owens, F. J.; Sharma, R.; Ahuja, R.; Guillen, J. M.; Johansson, B.; Gehring, G. A. Ferromagnetism above room temperature in bulk and transparent thin films of Mn-doped ZnO. *Nat. Mater.* **2003**, *2* (10), 673−677.

(33) Chen, R.; Luo, F.; Liu, Y.; Song, Y.; Dong, Y.; Wu, S.; Cao, J.; Yang, F.; N'Diaye, A.; Shafer, P.; Liu, Y.; Lou, S.; Huang, J.; Chen, X.; Fang, Z.; Wang, Q.; Jin, D.; Cheng, R.; Yuan, H.; Birgeneau, R. J.; Yao, J. Tunable room-temperature ferromagnetism in Co-doped two-dimensional van der Waals ZnO. *Nat. Commun.* **2021**, *12* (1), 3952.

(34) Thomas, D. G. The Exciton Spectrum of Zinc Oxide. *J. Phys. Chem. Solids* **1960**, *15* (1−2), 86−96.

(35) Xu, S. J.; Xiong, S. J.; Shi, S. L. Resonant coupling of bound excitons with LO phonons in ZnO: excitonic polaron states and Fano interference. *J. Chem. Phys.* **2005**, *123* (22), 221105.

(36) Antonius, G.; Chan, Y.-H.; Louie, S. G. Polaron spectral properties in doped ZnO and $SrTiO_3$ from first principles. *Phys. Rev. Res.* **2020**, *2* (4), No. 043296.

(37) Scott, J. F. Uv Resonant Raman Scattering in ZnO. *Phys. Rev. B* **1970**, *2* (4), 1209.

(38) Phan, T. L.; Vincent, R.; Cherns, D.; Dan, N. H.; Yu, S. C. Enhancement of multiple-phonon resonant Raman scattering in Co-doped ZnO nanorods. *Appl. Phys. Lett.* **2008**, *93* (8), No. 082110.

(39) Phan, T. L.; Vincent, R.; Cherns, D.; Nghia, N. X.; Ursaki, V. V. Raman scattering in Me-doped ZnO nanorods (Me = Mn, Co, Cu and Ni) prepared by thermal diffusion. *Nanotechnology* **2008**, *19* (47), 475702.

(40) Du, C. L.; Gu, Z. B.; You, Y. M.; Kasim, J.; Yu, T.; Shen, Z. X.; Ni, Z. H.; Ma, Y.; Cheng, G. X.; Chen, Y. F. Resonant raman spectroscopy of (Mn,Co)-codoped ZnO films. *J. Appl. Phys.* **2008**, *103* (2), No. 023521.

(41) Cerqueira, M. F.; Vasilevskiy, M. I.; Oliveira, F.; Rolo, A. G.; Viseu, T.; Ayres de Campos, J.; Alves, E.; Correia, R. Resonant Raman scattering in ZnO:Mn and ZnO:Mn:Al thin films grown by RF sputtering. *J. Phys.: Condens. Matter* **2011**, *23* (33), 334205.

(42) Damen, T. C.; Porto, S. P. S.; Tell, B. Raman Effect in Zinc Oxide. *Phys. Rev.* **1966**, *142* (2), 570−574.

(43) Serrano, J.; Widulle, F.; Romero, A. H.; Rubio, A.; Lauck, R.; Cardona, M. Dependence of phonon widths on pressure and isotopic mass: ZnO. *Phys. Status Solidi B* **2003**, *235* (2), 260−266.

(44) Mofor, A. C.; Reuss, F.; El-Shaer, A.; Kling, R.; Schlenker, E.; Bakin, A.; Ahlers, H.; Siegner, U.; Sievers, S.; Albrecht, M.; Schoch, W.; Limmer, W.; Eisenmenger, J.; Mueller, T.; Huebel, A.; Denninger, G.; Ziemann, P.; Waag, A. Magnetism in V-/Mn-doped ZnO layers fabricated on sapphire. *Appl. Phys. A: Mater. Sci. Process.* **2007**, *88* (1), 161−166.

(45) Samanta, K.; Dussan, S.; Katiyar, R. S.; Bhattacharya, P. Structural and optical properties of nanocrystalline $Zn_{1−x}Mn_xO$. *Appl. Phys. Lett.* **2007**, *90* (26), 261903.

(46) Scott, J. F.; Damen, T. C.; Leite, R. C. C.; Silfvast, W. T. Resonant Raman effect in the indirect gap semiconductor gallium phosphide. *Solid State Commun.* **1969**, *7* (13), 953−955.

(47) Bylsma, R. B.; Becker, W. M.; Kossut, J.; Debska, U.; Yoder-Short, D. Dependence of energy gap on x and T in $Zn_{1-x}Mn_xSe$: The role of exchange interaction. *Phys. Rev. B* **1986**, *33* (12), 8207−8215.

(48) Kayani, Z. N.; Anjum, M.; Riaz, S.; Naseem, S.; Zeeshan, T. Role of Mn in biological, optical, and magnetic properties ZnO nano-particles. *Applied Physics A-Materials Science & Processing* **2020**, *126* (3), 197.

(49) Martin, R. M.; Varma, C. M. Cascade Theory of Inelastic Scattering of Light. *Phys. Rev. Lett.* **1971**, *26* (20), 1241−1244.

(50) Yi, Y. Y.; Marmon, J. K.; Chen, Y. P.; Zhang, F.; Sheng, T.; Wijewarnasuriya, P. S.; Zhang, H. T.; Zhang, Y. Intrinsic Exciton-Phonon Coupling and Tuning in ZnTe Nanowires Probed by Resonant Raman Scattering. *Phys. Rev. Appl.* **2020**, *13* (1), No. 011001.